Dalton Transactions

A Protein Scaffold Enables Hydrogen Evolution for a Ni-bisdiphosphine Complex

Journal:	*Dalton Transactions*
Manuscript ID	DT-ART-09-2021-003295
Article Type:	Paper
Date Submitted by the Author:	28-Sep-2021
Complete List of Authors:	Laureanti, Joseph; Pacific Northwest National Lab, Physical Biosciences Su, Qiwen; Pacific Northwest National Lab Shaw, Wendy; Pacific Northwest National Lab,

COMMUNICATION

A Protein Scaffold Enables Hydrogen Evolution for a Ni-bisdiphosphine Complex

Received 00th January 20xx,
Accepted 00th January 20xx

DOI: 10.1039/x0xx00000x

Joseph A. Laureanti, Qiwen Su, Wendy J. Shaw[a]*

An artificial metalloenzyme acting as a functional biomimic of hydrogenase enzymes was activated by assembly via covalent attachment of the molecular complex, $[Ni(PN^{glycine}P)_2]^{2-}$, within a structured protein scaffold. Electrocatalytic H_2 production was observed from pH 3.0 to 10.0 for the artificial enzyme, while no electrocatalytic activity was observed for similar $[Ni(PNP)_2]^{2+}$ systems.

Enzymatic systems have the capacity to control every aspect of a catalytic reaction including: transition state stabilization, substrate delivery, product removal, geometry stabilization, proton and electron pathways, and control of allosteric and electrostatic effects.[1-5] This level of control is due to millions of years of optimization via evolutionary pressure. While the metal is critical to catalysis, the protein scaffold has also been shown to be critical to enzymatic performance by modulating proton relays, stabilizing active site structures, hydrophilic interactions, substrate/product transport, and long range interactions.[6-10] The relatively new field of creating artificial enzymes takes inspiration from nature with the aim of identifying/incorporating design principles from the protein scaffold of native enzymatic systems to capture some of these features. This approach allows us to better understand enzymatic design principles as well as improving synthetic catalysts.[11-17] An area of current relevance is improving electrocatalysts for energy related applications, which could enable the ability to store excess electrical energy in liquid fuels like hydrogen, ammonia, or methanol.[18-22]

In this work, we explore two design features: geometry stabilization and proton relays. A positioned proton relay is inspired by the metalloenzyme, hydrogenase. Hydrogenase catalyzes both H_2 production and H_2 oxidation reactions very fast and with very low energy input (i.e. low overpotential) at atmospheric pressures, ambient temperatures, and using earth abundant metals.[23] The pendant amine in the second coordination sphere of the H-cluster of [FeFe]-hydrogenase (Figure 1), is a key feature of efficient performance by serving to relay protons into and out of the active site. Mimicking this pendent amine in molecular catalysts has resulted in incredibly fast catalytic rates, low energy input, and

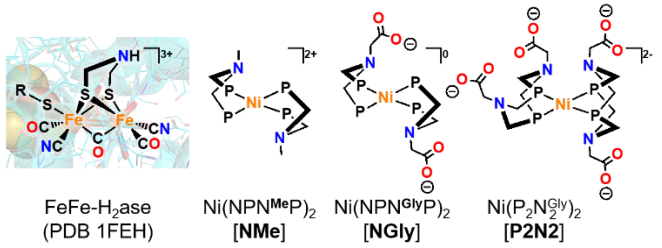

Figure 1. H-cluster from [FeFe]-hydrogenase (left) and biomimetic Ni complexes. The two $[Ni(PNP)_2]$ ([**NMe**] and [**NGly**], middle) and the $[Ni(P_2N_2)_2]$ ([**P2N2**], right) incorporate the design principle of a pendant base from hydrogenase enzymes.

catalytic reversibility.[10, 24-30] The $Ni(P_2N_2)_2$ systems have been particularly well-studied.[31] Comparison with complexes containing the analogous PNP ligands which are orders of magnitude slower[32] demonstrated that positioning of the pendant amine, enabled by the larger P_2N_2 ring system, is critical to their performance.[33-36] Specifically, it was found that restricting the ring flipping via geometry stabilization of the P_2N_2 ligand results in a dramatic increase in catalytic activity.[37]

Here, we used a protein scaffold rather than an organic ligand to limit the dynamics in the $Ni(PN^{Gly}P)_2$ system ([**NGly**]) to attempt to accelerate the H_2 oxidation above <1 s^{-1} observed for the $Ni(PN^{Me}P)_2$ molecular catalyst ([**NMe**]).[32] Instead of increasing H_2 oxidation, we found that embedding [**NGly**] in a protein scaffold enables electrocatalytic H_2 *production*, redirecting the activity and making it orders of magnitude faster. We employed a protein scaffold, LmrR, that can be produced in high yield, is amenable to a variety of amino acid point mutations, and has been proven to accommodate covalent attachment using Cu or Rh complexes.[38-44] We have previously used this system to produce a series of artificial

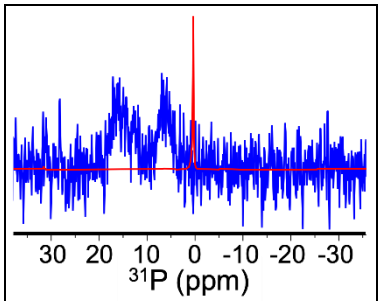

Figure 2. Phosphorus-31 NMR spectra showing $[Ni(PN^{Gly}P)_2]^{2-}$ (red trace) in a neat D_2O solution and $[Ni(PN^{Gly}P)_2]\subset$LmrR (blue trace) in 10 mM HEPES solution with 7% D_2O.

[a] *Physical and Computational Sciences Directorate, Pacific Northwest National Laboratory, Richland, WA 99352, USA*

† Footnotes relating to the title and/or authors should appear here.
Electronic Supplementary Information (ESI) available: [details of any supplementary information available should be included here]. See DOI: 10.1039/x0xx00000x

Scheme 1. A) Synthetic preparation of [Ni(PN^{Gly}P)$_2$] ([**NGly**]). B) Cartoon representation of the Ni complex. C) Cartoon representation of [Ni(PN^{Gly}P)$_2$]⊂LmrR. D) Molecular model produced using previously solved crystal structure of a similar complex containing Rh instead of Ni (PBD ID 6DO0).

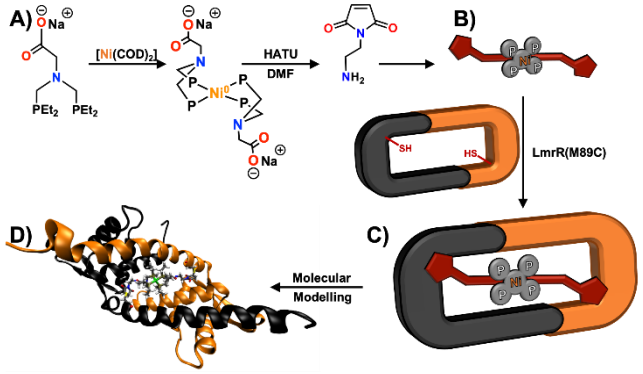

metalloenzymes capable of catalytic CO_2 hydrogenation at room temperature.[40, 44]

Expanding this system for H_2 production was completed by preparing a water soluble Ni-complex [**NGly**], Figure 1, using one equivalent of [Ni^0(COD)$_2$] with two equivalents of the PN^{Gly}P ligand, Scheme 1A, and was isolated using reported procedures.[44] The resulting ^{31}P NMR spectrum displayed a single resonance at 2.8 ppm in D_2O, Figure 2. The UV-Vis spectrum measured at pH 7 in a 0.1 M HEPES solution shows a transition at 348 nm with a measured extinction coefficient of 500 mM^{-1} cm^{-1}, Figure S1.

Immobilization of the Ni complex within the LmrR scaffold was facilitated via *in situ* amide bond formation of the maleimide linker, Scheme 1, followed by a Michael addition between the two maleimide groups of the [**NGly**] complex and the two cysteine residues of the homodimeric LmrR protein scaffold, Scheme 1A-C. Here, we employed an identical covalent attachment strategy in comparison to our previous work[40, 44] with [Rh(PN^{Gly}P)$_2$]⊂LmrR, and we obtained a similar product for the [Ni(PN^{Gly}P)$_2$]⊂LmrR assembly, Scheme 1D, based on absorbance spectroscopy, ^{31}P NMR spectroscopy, and electrospray-ionization mass spectrometry (ESI-MS). Covalent attachment of the PNP ligand to the LmrR protein scaffold was confirmed using ESI-MS, Figure S2. The ethyl phosphine ligands are extremely sensitive to O_2 and as a result the Ni metal is lost during ESI-MS experiments. However, an expected mass of one monomer + PNP ligand with maleimide linker is observed in the ESI-MS data, suggesting covalent attachment is indeed occurring. Absorbance spectroscopy was used to attempt determine the coupling efficiency (95 ±5%) of [**NGly**] to LmrR (mol Ni: mol LmrR dimer), using an experimentally derived extinction coefficient for [**NGly**] of 500 mM^{-1} cm^{-1}, Figure S1. However, there is a slight shift in the absorbance maxima for [Ni(PN^{Gly}P)$_2$]⊂LmrR, making the reported coupling efficiency an estimation. Phosphorous-31 NMR spectroscopy was also used to compare the free [**NGly**] complex to the assembled [Ni(PN^{Gly}P)$_2$]⊂LmrR and the resulting spectra shows two equal resonances (6.1 ppm and 15.4 ppm), both shifted downfield compared to the free [**NGly**] complex (2.8 ppm), Figure 2. This shift in the ^{31}P resonance suggests the coordination environment of the [**NGly**] complex has slightly less electron density, while the presence of two equal resonances indicates that the berry pseudo rotation observed for these complexes in solution has been hindered, an observation seen in the [Ni(P$_2$N$_2$)] complexes ([**P$_2$N$_2$**]).[37, 45, 46]

Cyclic voltammetry of the artificial enzyme demonstrated catalytic H_2 production. A 10 µL aliquot of [Ni(PN^{Gly}P)$_2$]⊂LmrR was deposited on an edge-plane pyrolytic graphite electrode (EPPG) surface, was interrogated by cycling the potential between 0 and -1.1 V vs. the standard hydrogen electrode (SHE), Figure 3A. Films of [Ni(PN^{Gly}P)$_2$]⊂LmrR are not stable at EPPG or glassy carbon and diminish after the first cycle. Therefore, a single film was not used for all experiments. Instead, a single film was employed for each pH unit. After polishing and applying a new 10 µL aliquot film of [Ni(PN^{Gly}P)$_2$]⊂LmrR, current enhancement was observed for the [Ni(PN^{Gly}P)$_2$]⊂LmrR films compared to a blank EPPG electrode from pH 3.0 to 10 when cycling to negative potentials. Experiments in which no protein was applied to the electrode surface are shown in Figure 3A as a dotted black line at pH 10.0, and background cyclic voltammograms are shown in Figure S3.

The activity of the [Ni(PN^{Gly}P)$_2$]⊂LmrR assembly has a lower estimate of 120 s^{-1} at pH 3 determined using Equation 1,

$$TOF = \frac{i_p}{nFA\Gamma} \qquad \text{Equation 1}$$

where i_p is the background subtracted peak current from the linear sweep voltammogram, n is the number of electrons, F is Faraday's constant, A is the area of the electrode surface, and Γ is the electrode surface coverage of the [Ni(PN^{Gly}P)$_2$]⊂LmrR film. Direct measurement of the surface coverage could not be completed as a non-turnover transition was not observed, therefore the following assumptions are made for the film coverage: ratio of [Ni(PN^{Gly}P)$_2$]:LmrR dimer = 1:1, electrode area = 0.07 cm^2, area of one [Ni(PN^{Gly}P)$_2$]⊂LmrR = 5x10^{-10} cm^2, and a final surface coverage for [Ni(PN^{Gly}P)$_2$]⊂LmrR = 3.2 pmol/cm^2 , assuming close packing of the dimer on its side on the surface. The values presented in Figure 3B provide an estimate for the turnover frequency (TOF) as a function

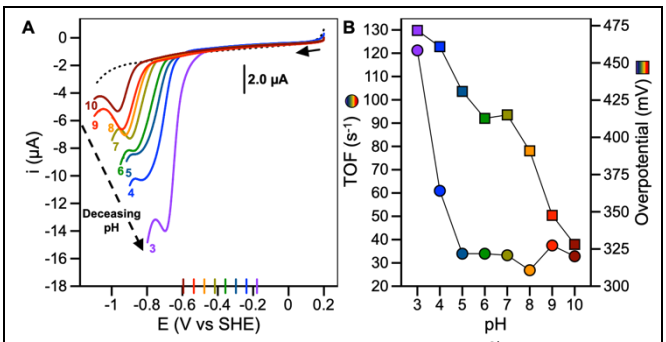

Figure 3 A) Linear sweep voltammetry of a [Ni(PN^{Gly}P)$_2$]⊂LmrR film on edge plane pyrolytic graphite (EPPG). The buffer used was 100 mM phosphate titrated to the designated pH value. Solid black arrow denotes initiation and scan direction. Dashed black arrow displays the decrease and cathodic shift of the peak current for each voltammogram from acidic, pH 3, to basic, pH 10, conditions. Colored bars on the X-axis denote the thermodynamic potential for H_2 evolution and correspond to the respective voltammograms. B) Overpotential (squares) and estimated turn over frequencies (TOF, circles) resulting from the baseline subtracted linear sweep voltammograms in A. The following color scheme was used: pH 3.0 (purple), 4.0 (navy), 5.0 (blue), 6.0 (green), 7.0 (asparagus), 8.0 (orange), 9.0 (red), 10.0 (crimson).

of pH, with the greatest TOF = 120 s^{-1} at pH 3 and declining down to pH 10.0 (30 s^{-1}).

The software package QSOAS[47] was used to generate the values for $E_{cat/2}$ and to subtract the background to obtain the i_p values, which are both shown for each pH value in Figure S4. The $E_{cat/2}$ values cathodically shift by 40 mV per decade from pH 3.0 to 10.0 (R^2 = 0.99), Figure S4 (circles). Baseline subtraction of the linear sweep voltammograms produce peak current (i_p) minima, Figure S4 (squares), that show two regimes: 1) where there is a sharp drop in activity from pH 3.0 to 5.0, and 2) peak currents independent of pH from pH 6.0 to 10.0. The peak current and $E_{cat/2}$ data suggests proton coupled electron transfer from pH 3 to pH 5.[48] Implying protonation of the metallocenter or an outer-sphere amino acid residue. Both carboxylic acids and at least one amine have been shown to be protonated in the analogous [**P2N2**] complexes at low pH, consistent with the observation for the [Ni($PN^{Gly}P$)$_2$]⊂LmrR complex, suggesting that it is the ligand and not the metal that is protonated.[26, 49] At pH >5.0, deprotonation of the pendant amine and/or the carboxylic acid hinder proton transfer, leading to decreased proton reduction capacity, as has been observed previously for the related [**P2N2**].[49]

When compared to the [**P2N2**] reactivity, it is clear that positioning of the pendant amine with an organic scaffold instead of the protein scaffold used here have different effects. Specifically, the [**P2N2**] was active for both H_2 oxidation and H_2 production under similar conditions to those used here, albeit with a different proton source, while this artificial enzyme is only active for H_2 production. In addition, the H_2 production rate of the artificial enzyme is over an order of magnitude slower than the [**P2N2**] electrocatalyst.[49] Although the rate of catalytic turnover for the [**P2N2**] system proved to be higher, the overpotential was lower for [Ni($PN^{Gly}P$)$_2$]⊂LmrR. This trade-off is generally observed where a lower thermodynamic driving force, i.e. a lower overpotential often results in a lower catalytic rate, while faster catalytic rates are accompanied by a larger thermodynamic driving force.[50] As an example, at pH 5 the [**P2N2**] showed a rate of ~250 s^{-1} and an overpotential of +500 mV, while [Ni($PN^{Gly}P$)$_2$]⊂LmrR had a rate of 30 s^{-1} and an overpotential of +425 mV.

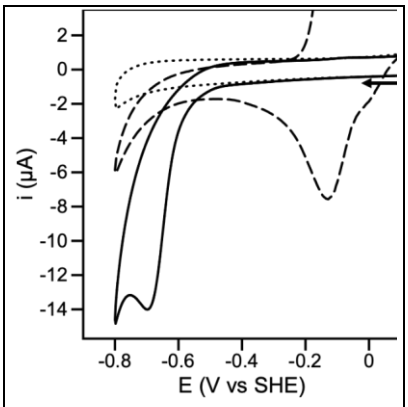

Figure 4. Comparison of current response using cyclic voltammetry for [Ni($PN^{Gly}P$)$_2$]⊂LmrR (solid trace) and [**NGly**] (dashed trace) with a sweep rate of 20 mV s^{-1} at pH 3.0. The rapid increase in current at ~-0.5 V for the [Ni($PN^{Gly}P$)$_2$]⊂LmrR is indicative of catalytic activity for H_2 production. A blank cyclic voltammogram for EPPG in the same buffer is shown as the dotted trace.

While the lower overpotential is likely a factor, there are several other potential contributors for the observed order of magnitude decrease in catalytic H_2 production: 1) the pocket of the protein dimer interface does not position the pendant amine as optimally to the metal as the P_2N_2 ligand, and/or 2) the pocket does not limit the ring flips of the six membered ring that contains the pendant amine, decreasing the time it sits in the preferred location. Further studies are needed to understand the differences in these two systems.

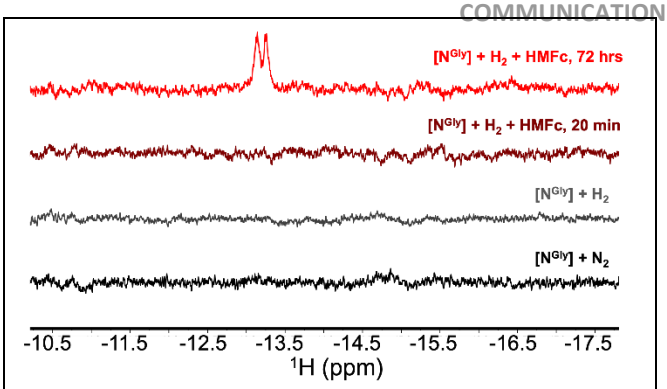

Figure 5. Hydride formation by [**NGly**] from oxidation of H_2 at pH 7. A hydride species is observed at -13.2 ppm, demonstrating H_2 addition and a preference of the parent complex for H_2 oxidation.

The complex without the scaffold, [**NGly**], was not found to be electrocatalytic based on cyclic voltammetry experiments collected over the same pH range (Figure S5). Experiments from pH 3 to 8, were cycled between +0.2 to -0.6 V vs SHE. In this regime, one reversible pair of anodic and cathodic transitions are observed that shift cathodically as the pH is increased to more basic conditions; $E_{1/2}$ values for these transitions are shown in the inset in Figure S5. Starting at pH 7 the cathodic wave becomes broader suggesting a second overlapping process is occurring from neutral to basic conditions. Similar behaviour was observed for the [$\mathbf{P_2N_2}$] electrocatalyst when starting from the Ni^0 species. Specifically , two irreversible reductions were found at pH 7 while a reversible pair of oxidation and reduction events are observed at pH 5.[49] This second irreversible process is clearly observed from pH 8 to 10 for [**NGly**]. In Figure 4, the H_2 evolution activity at pH 3 of the film of [Ni($PN^{Gly}P$)$_2$]⊂LmrR (solid trace) is compared to the non-catalytic wave of parent [**NGly**] complex (dashed trace) alone in solution. A current enhancement is clearly observed for the artificial enzyme with ~470 mV overpotential, while the [**NGly**] complex alone does not show current enhancement until potentials outside the solvent window are reached. The activation of H_2 production activity demonstrates that the protein scaffold has a beneficial impact on catalysis.

Although H_2 production was enabled by the protein scaffold, H_2 oxidation was not. Oxidation of H_2 was expected for [**NGly**] based upon previous studies showing [**NMe**] to add H_2 in aqueous environments.[32] Electrocatalytic H_2 oxidation activity was not observed for the [**NGly**] complex. However, incubating the Ni^0 complex with hydroxymethyl ferrocene under 1 atm of H_2 led to the non-catalytic formation of a Ni-H species after ~72 hours of incubation, Figure 5, suggesting a thermodynamic preference of the parent [**NGly**] complex to oxidize rather than evolve H_2.[36] Further studies are needed to understand how the scaffold is enabling a redirection of the catalytic preference from very slightly favoring H_2 oxidation to significantly favoring H_2 production.

In conclusion, an artificial metalloenzyme capable of electrocatalytic H_2 production from acidic (pH 3.0) to basic (pH 10.0) conditions was produced via covalent attachment of a non-catalytic Ni-bisdiphospine complex in the LmrR protein scaffold. Instead of enhancing H_2 oxidation, expected based on the behaviour of related Ni-PNP complexes, [Ni($PN^{Gly}P$)$_2$]⊂LmrR was shown to produce H_2.

The [**NGly**] complex produced herein is water soluble, but was not electrocatalytic for H_2 production or oxidation under any conditions at which the [Ni($PN^{Gly}P$)$_2$]⊂LmrR system was electrocatalytic. Of interest is that the scaffold did not appear to position the pendant amine as effectively as the organic P_2N_2 ligand, which showed bidirectionality, and much faster H_2 production catalysis.[49] Clearly, the LmrR protein scaffold is influencing the catalytic activity of the immobilized [Ni($PN^{Gly}P$)$_2$] molecular complex. It is likely that the immobilization invokes a strained conformation that positions the pendant amine more appropriately for catalytic turn-over, enabling a proton transfer pathway; a conformation that the parent complex is unable to achieve while diffusing through solution.

Experimental

General. All chemicals purchased were of the highest quality available and used without further purification. Standard Schlenk line techniques or a Vacuum Atmospheres (VacAtm) glovebox were used under an inert atmosphere of nitrogen for all chemical manipulations. An Agilent NMRS 500 MHz spectrometer was used to collect all nuclear magnetic resonance (NMR) data. Phosphoric acid (85%, 0 ppm) was used to reference all ^{31}P NMR data. Protein concentration was determined using a NanoDrop spectrophotometer (ThermoScientific NanoDrop 2000c) with a calculated extinction coefficient of 19940[51]. An Ocean Optics modular USB2000+ spectrophotometer (Largo, Florida, USA) with a DT-Mini-2-GS light source containing deuterium and tungsten lamps was employed inside the VacAtm glovebox to collect UV-Visible data. Cyclic voltammetry experiments were referenced to the standard hydrogen electrode (SHE) from Ag/AgCl by addition of hydroxymethyl ferrocene following electrochemical experiments.[52]

Ligand Preparation. Bis(hydroxymethyl)diethylphosphine and Bis(diethylphosphinomethyl)glycine ($PN^{Gly}P$) were synthesized and purified as previously detailed.[53]

Metalation. The [Ni(COD)$_2$] starting material (0.1 mmole, 0.5 equivalents), dissolved in acetonitrile, was introduced by dropwise addition to a rapidly stirring suspension of 0.2 mmoles of $PN^{Gly}P$ ligand in THF. The suspension was stirred for 30 minutes before the solvent was removed to about 1 mL, precipitated with diethylether, collected on a celite column, washed with 10 mL diethyl ether, and eluted with ethanol to afford a yellow solution. The solvent was then removed under reduced pressure. ^{1}H NMR (500 MHz, D_2O): δ 1.04 (24H), 1.37 – 1.82 (16H), 3.0 – 3.27 (12H). ^{31}P{1 H} NMR (202 MHz, D_2O): δ: 2.88 (s).

Cell Growth, Protein Expression, and Protein Purification. The plasmid for expression was ordered from ATUM (Newark, CA) in lactose inducible pJ414 vectors containing ampicillin resistance for selection. The native LmrR sequence was amended with three base point mutations: K55D, K59Q and M89C and was purified according to the previously reported protocols.[40, 53]

Assembly of [Ni($PN^{Gly}P$)$_2$]⊂LmrR(M89C). Purified LmrR(M89C) (250 - 300 nmol) was passed through a PD-10 desalting column (GE HealthCare, Marlborough, MA, USA) equilibrated with 4-(2-hydroxyethyl)-1- piperazineethanesulfonic acid (HEPES, 0.1 M, pH 7.0). The eluent was further diluted with the same buffer to a final protein concentration equal to 10 µM and allowed to stir. Concomitantly, a dimethylformamide (DMF) solution containing N-[(Dimethylamino)]-1H1,2,3-triazolo-[4,5-b]pyridin-1-ylmethylene]-N-methylmethanaminium hexafluorophosphate (1.65 µmol, HATU) and diisopropylethylamine (1.65 µmol, DIPEA) was added to solid *[Ni($PN^{Gly}P$)$_2$]* and allowed to stir for 15 minutes. Amide bond formation with N-(2-Aminoethyl)maleimide (1.88 µmol) was allowed to proceed for 15 minutes before the mixture was added to a vigorously stirring protein solution of LmrR(M89C). Covalent attachment of the Ni complex at LmrR was allowed to proceed for 30 minutes. Millipore centrifugal spin filters (0.5 mL, 3 kDa NMWCO) were employed to concentrate the reaction to < 0.5 mL before application to a NAP-5 column (GE HealthCare, Marlborough, MA, USA) equilibrated with HEPES (0.1 M, pH 7.0) to remove unbound complex. Eluted products were either stored at -35 °C or used immediately for spectroscopic or catalytic experiments. ESI: ^{15}N-LmrR + $PN^{gly\rightarrow mal}P$ ligand + H, calculated = 14187.20, found = 14187.13. ^{31}P{1 H} NMR (202 MHz, D_2O): δ: 6.2 and 16.2 (br); required collection for 72 hours at 700 MHz ^{1}H frequency due to the low concentration and broad resonances. Line broadening was applied at 20 Hz for processing.

Electrochemical Analysis. A standard three-electrode cell was used for cyclic voltammetry experiments and consisted of either an Edge Plane Pyrolytic Graphite (EPPG, 2 mm diameter) or a glassy carbon working electrode (1 mm diameter), a Ag/AgCl (3.5 M KCl) reference electrode, and a glassy carbon rod (3 mm diameter) as the counter electrode. Protein film voltammetry was conducted by spotting 10 µL of a 500 µM solution of [Ni($PN^{Gly}P$)$_2$]⊂LmrR(M89C) directly onto the 2 mm EPPG electrode surface and allowed to dry before introduction to the electrochemical cell. The potential was then cycled between 0 and -1.3 V vs SHE at a scan rate of 0.02 V s^{-1}. Due to the instability of the film for >1 cycle, we report only the first scan.

The cyclic voltammetry for [**NGly**] was completed in a 1.0 mM solution by dissolving solid [**NGly**] in the appropriate volume of phosphate buffer at the required pH. A standard three electrode cell was used for [**NGly**] cyclic voltammograms.

Overpotential Calculation: The overpotential was calculated using the absolute value from equation 1. The program QSOAS was used to background subtract the linear sweep voltammograms and to calculate the first derivative. The potential at the maxima of the derivative was chosen as the $E_{cat/2}$ value.

$$\eta = E_{cat/2} - (-59.5\,mV * pH) \qquad \text{Equation 1}$$

Hydride formation by [Ni($PN^{Gly}P$)$_2$ in the presence of hydroxymethyl ferrocene. In a glovebox, [**NGly**] complex was loaded into a J-Young tube in 0.1 M HEPES pH 7.0, the headspace gas was exchanged for H_2. The J-Young tube was then brought back into the glovebox, 2 eq of hydroxymethylferrocene (HMFc) were added, the J-Young tube was sealed, brought out of the glovebox, recharged with 1 atm of H_2, and mixed vigorously before recording the ^{1}H NMR spectrum.

Conflicts of interest

There are no conflicts to declare

Acknowledgements

This work was supported by the U.S. Department of Energy (DOE), Office of Science, Office of Basic Energy Sciences (BES), Division of Chemical Sciences, Geosciences & Biosciences and in part by the U.S.

DOE, Office of Science, Office of Workforce Development for Teachers and Scientists (WDTS) under the Science Undergraduate Laboratory Internships Program (SULI) and performed in part using the William R. Wiley Environmental Molecular Sciences Laboratory, a U.S. DOE national scientific user facility sponsored by the DOE's Office of Biological and Environmental Research and located at the Pacific Northwest National Laboratory (PNNL). Battelle operates PNNL for the U.S. DOE.

References

1. P. K. Agarwal, *Biochemistry*, 2019, **58**, 438-449.
2. K. Chen and F. H. Arnold, *Nature Catalysis*, 2020, **3**, 203-213.
3. T. Vornholt and M. Jeschek, *ChemBioChem*, 2020, **21**, 2241-2249.
4. A. E. Donnelly, G. S. Murphy, K. M. Digianantonio and M. H. Hecht, *Nature Chemical Biology*, 2018, **14**, 253-255.
5. V. Nanda and R. L. Koder, *Nature Chemistry*, 2010, **2**, 15-24.
6. J. H. Artz, O. A. Zadvornyy, D. W. Mulder, S. M. Keable, A. E. Cohen, M. W. Ratzloff, S. G. Williams, B. Ginovska, N. Kumar, J. Song, S. E. McPhillips, C. M. Davidson, A. Y. Lyubimov, N. Pence, G. J. Schut, A. K. Jones, S. M. Soltis, M. W. W. Adams, S. Raugei, P. W. King and J. W. Peters, *J Am Chem Soc*, 2020, **142**, 1227-1235.
7. J. T. Kellis, R. J. Todd and F. H. Arnold, *Bio/Technology*, 1991, **9**, 994-995.
8. A. Chatzigoulas and Z. Cournia, *WIREs Computational Molecular Science*, 2021, **n/a**, e1529.
9. L. J. Kingsley and M. A. Lill, *Proteins*, 2015, **83**, 599-611.
10. J. A. Laureanti, M. O'Hagan and W. J. Shaw, *Sustainable Energy & Fuels*, 2019, **3**, 3260-3278.
11. C. M. Thomas and T. R. Ward, *Chem Soc Rev*, 2005, **34**, 337-346.
12. B. d. P. Mariz, S. Carvalho, I. L. Batalha and A. S. Pina, *Organic & Biomolecular Chemistry*, 2021, **19**, 1915-1925.
13. R. E. Treviño, J. W. Slater and H. S. Shafaat, *ACS Applied Energy Materials*, 2020, **3**, 11099-11112.
14. I. Drienovská and G. Roelfes, *Nature Catalysis*, 2020, **3**, 193-202.
15. F. Schwizer, Y. Okamoto, T. Heinisch, Y. Gu, M. M. Pellizzoni, V. Lebrun, R. Reuter, V. Köhler, J. C. Lewis and T. R. Ward, *Chem Rev*, 2018, **118**, 142-231.
16. H. J. Davis and T. R. Ward, *ACS Cent Sci*, 2019, **5**, 1120-1136.
17. I. D. Petrik, J. Liu and Y. Lu, *Current opinion in chemical biology*, 2014, **19**, 67-75.
18. M. Grasemann and G. Laurenczy, *Energy & Environmental Science*, 2012, **5**, 8171-8181.
19. J. A. Turner, *Science*, 2004, **305**, 972.
20. N. S. Lewis and D. G. Nocera, *Proceedings of the National Academy of Sciences*, 2006, **103**, 15729.
21. D. Gust, T. A. Moore and A. L. Moore, *Accounts of Chemical Research*, 2009, **42**, 1890-1898.
22. R. K. Pieter Tans, Global Monitoring Laboratory, https://www.esrl.noaa.gov/gmd/ccgg/trends, 2020).
23. W. Lubitz, H. Ogata, O. Rüdiger and E. Reijerse, *Chem Rev*, 2014, **114**, 4081-4148.
24. B. Ginovska-Pangovska, A. Dutta, M. L. Reback, J. C. Linehan and W. J. Shaw, *Acc. Chem. Res.*, 2014, **47**, 2621-2630.
25. G. Caserta, S. Roy, M. Atta, V. Artero and M. Fontecave, *Curr Opin Chem Biol*, 2015, **25**, 36-47.
26. A. Dutta, D. L. DuBois, J. A. S. Roberts and W. J. Shaw, *Proceedings of the National Academy of Sciences*, 2014, **111**, 16286-16291.
27. M. Rakowski DuBois and D. L. DuBois, *Chem. Soc. Rev.*, 2009, **38**, 62-72.
28. D. L. Dubois, *Inorganic Chemistry*, 2014, **53**, 3935-3960.
29. D. Schilter, J. M. Camara, M. T. Huynh, S. Hammes-Schiffer and T. B. Rauchfuss, *Chem Rev*, 2016, **116**, 8693-8749.
30. T. R. Simmons, G. Berggren, M. Bacchi, M. Fontecave and V. Artero, *Coordination Chemistry Reviews*, 2014, **270-271**, 127-150.
31. M. O'Hagan, M.-H. Ho, J. Y. Yang, A. M. Appel, M. R. DuBois, S. Raugei, W. J. Shaw, D. L. DuBois and R. M. Bullock, *J. Am. Chem. Soc.*, 2012, **134**, 19409-19424.
32. C. J. Curtis, A. Miedaner, R. Ciancanelli, W. W. Ellis, B. C. Noll, M. Rakowski DuBois and D. L. DuBois, *Inorg. Chem.*, 2003, **42**, 216-227.
33. Y. A. Small, D. L. DuBois, E. Fujita and J. T. Muckerman, *Energy Environ. Sci.*, 2011, **4**, 3008.
34. S. Raugei, S. Chen, M.-H. Ho, B. Ginovska-Pangovska, R. J. Rousseau, M. Dupuis, D. L. DuBois and R. M. Bullock, *Chem. Eur. J.*, 2012, **18**, 6493-6506.
35. A. Dutta, A. M. Appel and W. J. Shaw, *Nature Reviews Chemistry*, 2018, DOI: papers2://publication/doi/10.1038/s41570-018-0032-8, 1-9.
36. D. L. DuBois and R. M. Bullock, *Eur. J. Inorg. Chem.*, 2011, **2011**, 1017-1027.
37. A. J. P. Cardenas, B. Ginovska, N. Kumar, J. Hou, S. Raugei, M. L. Helm, A. M. Appel, R. M. Bullock and M. O'Hagan, *Angew. Chem.*, 2016, **128**, 13707-13711.
38. G. Roelfes, *Accounts of chemical research*, 2019, **52**, 545-556.
39. L. Alonso-Cotchico, J. Rodríguez-Guerra Pedregal, A. Lledós and J.-D. Maréchal, *Frontiers in Chemistry*, 2019, **7**, 211.
40. J. A. Laureanti, B. Ginovska, G. W. Buchko, G. K. Schenter, M. Hebert, O. A. Zadvornyy, J. W. Peters and W. J. Shaw, *Organometallics*, 2020, DOI: 10.1021/acs.organomet.9b00843.
41. I. Drienovská, R. A. Scheele, C. Gutiérrez de Souza and G. Roelfes, *Chembiochem : a European journal of chemical biology*, 2020, **21**, 3077-3081.
42. J. Bos, F. Fusetti, A. J. M. Driessen and G. Roelfes, *Angew. Chem. Int. Ed.*, 2012, **51**, 7472-7475.
43. J. Bos and G. Roelfes, *Curr Opin Chem Biol*, 2014, **19**, 135-143.
44. J. A. Laureanti, G. W. Buchko, S. Katipamula, Q. Su, J. C. Linehan, O. A. Zadvornyy, J. W. Peters and M. O'Hagan, *ACS Catalysis*, 2019, **9**, 620-625.
45. J. A. Franz, M. O'Hagan, M.-H. Ho, T. Liu, M. L. Helm, S. Lense, D. L. DuBois, W. J. Shaw, A. M. Appel, S. Raugei and R. M. Bullock, *Organometallics*, 2013, **32**, 7034-7042.
46. S. Hammes-Schiffer, *J Am Chem Soc*, 2015, **137**, 8860-8871.
47. V. Fourmond, *Analytical Chemistry*, 2016, **88**, 5050-5052.
48. J.-M. Savéant, *Energy & Environmental Science*, 2012, **5**, 7718-7731.

49. A. Dutta, S. Lense, J. Hou, M. H. Engelhard, J. A. S. Roberts and W. J. Shaw, *J. Am. Chem. Soc.*, 2013, **135**, 18490-18496.
50. C. M. Klug, A. J. P. Cardenas, R. M. Bullock, M. O'Hagan and E. S. Wiedner, *ACS Catal.*, 2018, **8**, 3286-3296.
51. E. Gasteiger, C. Hoogland, A. Gattiker, S. Duvaud, M. R. Wilkins, R. D. Appel and A. Bairoch, in *The Proteomics Protocols Handbook*, Humana Press, 2005, ch. 52, pp. 571-607.
52. P. Rodriguez-Maciá, A. Dutta, W. Lubitz, W. J. Shaw and O. Rüdiger, *Angew. Chem. Int. Ed.*, 2015, **127**, 12303-12307.
53. J. A. Laureanti, G. W. Buchko, S. Katipamula, Q. Su, J. C. Linehan, O. A. Zadvornyy, J. W. Peters and M. O'Hagan, *ACS Catalysis*, 2018, **9**, 620-625.